



Integration of a Nonlinear Vibration Absorber and Levitation Magnetolectric Energy Harvester for Whole-Spacecraft Systems

Ye-Wei Zhang^{1*}  Shi-Lei Wang¹ Zhi-Yu Ni¹ Zhi-Wei Fang² Jian Zang¹ Bo Fang¹

⁽¹⁾ College of Aerospace Engineering, Shenyang Aerospace University, Shenyang 110136, China)

⁽²⁾ Shanghai Prime Machinery Company Limited, Shanghai 200072, China)

Received 28 October 2018; revision received 16 January 2019; Accepted 23 January 2019;
published online 11 February 2019

© The Chinese Society of Theoretical and Applied Mechanics 2019

ABSTRACT This paper presents a new device integrating a nonlinear vibration absorber with a levitation magnetolectric energy harvester for whole-spacecraft systems. This device effectively reduces vibration and has a stronger energy harvesting capability than the existing systems. It harvests energy from a wide frequency range and has a high output voltage. The harvested energy is determined by magnetic field strength, excitation frequency, and resistive load. The change in the magnetic field strength has the least impact on the output voltage. The vibration reduction effects and harvested energy of the system are analyzed with an approximate analytical method that combines the harmonic balance approach and the pseudo-arclength continuation algorithm. The results of the Runge–Kutta method are nearly consistent with those of the approximate analytical method. Moreover, the effects of the excitation frequency, resistive load, and parameters of the nonlinear energy sink on the system vibration response and energy harvesting are analyzed.

KEY WORDS Levitation magnetolectric energy harvester, Whole spacecraft, Nonlinear energy sink, Vibration reduction

1. Introduction

Spacecraft systems are subjected to harsh vibration environments before they enter their intended orbit. As a result, the spacecraft structure and the instruments in it may be easily damaged. Whole-spacecraft vibration reduction is an effective method to overcome this problem, and it has been widely used in recent years [1]. Johnson et al. [2] reported that vibration reduction in the SoftRide MultiFlex whole-spacecraft vibration isolation system is effective. Liu et al. [3, 4] optimized the design of an octo-strut platform to improve low longitudinal stiffness, which could effectively improve the dynamic vibration environment of spacecraft. Hu et al. [5] designed a control system that effectively suppresses system vibration and achieves accurate attitude control of spacecraft. However, the natural frequencies of most whole-spacecraft vibration reduction systems have changed, and these systems have limited vibration reduction effects.

The nonlinear energy sink (NES) is a new type of nonlinear vibration absorber that uses target energy transfer to suppress vibration. NES can remarkably reduce vibration without changing the

* Corresponding author. E-mail: zhangyewei1218@126.com

natural frequency [6–9]. Georgiades et al. [10] studied the vibration of NES connected to a damped and forced dispersive linear finite rod and discovered that NES is highly effective as a passive broadband energy absorber. Ahmadabadi and Khadem [11] investigated the effect of grounded and ungrounded NES on the vibration reduction of a cantilever beam and obtained 89% energy dissipation of the ungrounded system by optimizing the NES parameters. Chen et al. [12] proved that the vibration of a truss-core sandwich beam combined with NES exhibits excellent vibration suppression. Gourc et al. [13] analyzed the dynamic response of NES under harmonic excitation through experiments and confirmed the good vibration reduction effect of NES. Zang and Chen [14] revealed the dynamic complexity of NES by employing the harmonic balance approach and pseudo-arclength continuation algorithm. Dai et al. [15] studied the effects of NES on the amplitude of an elastically mounted square prism subjected to a galloping force and concluded that NES with optimized parameters can effectively reduce vibration. In addition, NES can effectively reduce the vibration of the transmission input shaft in an automotive drivetrain over a wide frequency range [16]. NES absorbs the vibration energy of the system to reduce vibration effectively. Moreover, the vibration energy can be absorbed as electric energy, which presents a meaningful research direction.

Researchers have also conducted extensive research on vibration-type energy harvesters [17–19]. Designed by Ferrari et al. [20], a nonlinear bistable piezoelectric converter for vibration reduction was tested on a cantilever beam and eventually harvested large amounts of energy during broadband vibration. Tao et al. [21] designed an electret-based micro-electro-mechanical system (MEMS) energy harvester that enables energy harvesting over a wider bandwidth compared with traditional linear systems. The flexible longitudinal zigzag structure of piezoelectric materials can efficiently collect energy at low frequencies [22]. Liu et al. [23] studied an electromagnetic energy harvester that generates current in copper coils through the law of electromagnetic induction. The highest open circuit voltage is 2.64 V. Zhou and Zuo [24] analyzed an asymmetric tristable energy harvester by using the harmonic balance approach, and the performance of the energy harvester was improved by changing the unstable equilibrium point. Chtiba et al. [25] connected NES to a piezoelectric device in a linear main structure; the system absorbed the vibrational energy of the simply supported beam, while the vibrational energy was converted into electrical energy. A system that consists of NES and a piezoelectric harvester can reduce vibration and harvest large amounts of energy if the system parameters are optimized [26]. Fang combined NES with a giant magnetostrictive material to reduce vibration and harvest energy. The highest voltage (1.79 V) was obtained at the resonant frequency, but no electrical energy was harvested at other frequencies [27, 28]. The capability of an energy harvesting system with NES was verified through an experiment by Kremer and Liu [29, 30]. In these studies, the systems can only harvest energy at natural frequency or low frequencies and have low output voltage. Therefore, the power-generating capability and frequency range of energy harvesters should be improved in the future.

In this work, we study the integration of NES and a novel levitation magnetoelectric energy harvester (MEEH) for vibration control and energy harvesting in whole-spacecraft systems. The MEEH consists of a magnetoelectric laminate and three ring magnets. It generates power on the resistive load through the magnetostrictive effect and the piezoelectric effect [31]. The laminated structure is a piezoelectric layer (PZT) bonded between two magnetostrictive layers (Terfenol-D) [32]. This system exhibits good vibration reduction and achieves a high voltage over a wide frequency range. A simplified mathematical model of the system is established in Sect. 2. Section 3 analyzes the response of the system and the harvested energy by using the harmonic balance approach and pseudo-arclength continuation algorithm. Section 4 discusses the effects of different parameters on system vibration response and energy harvesting. Section 5 provides the conclusions of this work.

2. Whole-Spacecraft Model with NES and MEEH

The equivalent simplified model of a whole spacecraft with NES and MEEH is shown in Fig. 1, where m_1 and m_2 are, respectively, the masses of the primary system and the subsystem [33]; k_i and c_i ($i = 1, 2$) are the linear stiffness and damping coefficients, respectively. NES is attached to mass m_2 and includes mass m_3 , cubic nonlinear stiffness coefficient k_3 , and damping coefficient c_3 . The energy harvester is placed on mass m_3 , and the intermediate magnet is rigidly connected to mass m_2 . Mass m_2 includes the mass of the middle magnet, and mass m_3 includes the mass of the energy harvester except for the middle magnet.

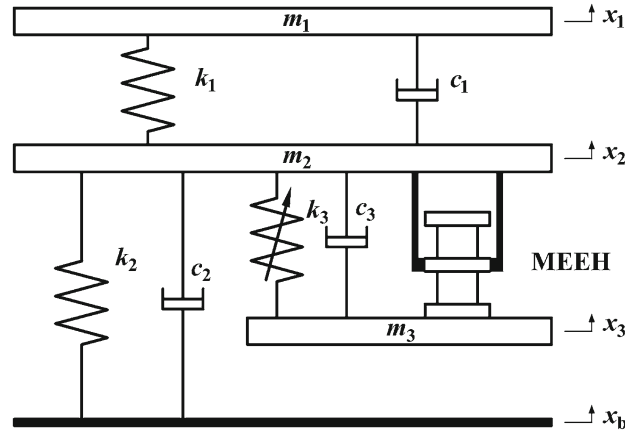


Fig. 1. Model of the whole-spacecraft system with NES and MEEH

The dynamic equation of the system is expressed as follows:

$$\begin{aligned}
 m_1 \ddot{x}_1 + c_1(\dot{x}_1 - \dot{x}_2) + k_1(x_1 - x_2) + m_1 \ddot{x}_b &= 0 \\
 m_2 \ddot{x}_2 + c_1(\dot{x}_2 - \dot{x}_1) + c_2 \dot{x}_2 + c_3(\dot{x}_2 - \dot{x}_3) + k_1(x_2 - x_1) + k_2 x_2 + k_3(x_2 - x_3)^3 - F_m + m_2 \ddot{x}_b &= 0 \\
 m_3 \ddot{x}_3 + c_3(\dot{x}_3 - \dot{x}_2) + k_3(x_3 - x_2)^3 + F_m + m_3 \ddot{x}_b &= 0
 \end{aligned} \quad (1)$$

where x_b is the excitation acceleration and F_m is the magnetic field force of the intermediate magnet [31].

$$\begin{aligned}
 x_b &= \frac{A_b}{(2\pi f)^2} \sin(2\pi f t) \\
 \dot{x}_b &= \frac{A_b}{2\pi f} \cos(2\pi f t) \\
 \ddot{x}_b &= -A_b \sin(2\pi f t)
 \end{aligned} \quad (2)$$

$$F = Az + Bz^3 = A(x_2 - x_3) + B(x_2 - x_3)^3 \quad (3)$$

where $A_b = 0.3$ g, $A = 6.39$ N/m, and $B = 1.66 \times 10^5$ N/m; f is the excitation frequency; and z is the central magnet relative displacement.

The output voltage and power of MEEH are

$$V = \frac{\varphi_m \varphi_p R_{\text{load}} H}{\varphi_p^2 R_{\text{load}} + (1 + j\omega R_{\text{load}} C_0) Z} \quad (4)$$

$$P = \frac{V^2}{R_{\text{load}}} \quad (5)$$

where φ_m is the magnetoelastic coupling factor; φ_p is the electromechanical coupling factor; C_0 is the static capacitance of PZT; Z is the equivalent mechanical impedance of the laminate composite; R_{load} is the resistive load; and H is the magnetic field strength, which can be expressed as $H = f(z) = f(x_2 - x_3)$ [31].

The energy harvested by the harvester is an alternating current. Its instantaneous voltage value is the real part of the complex voltage.

$$V_{\text{real}} = \frac{-A_1 A_2 H}{A_2^2 + \frac{A_3^2}{(2\pi f)^2}} \quad (6)$$

$$\begin{aligned}
 A_1 &= 2bt_p^2 d_{33,m} d_{31,p} R_{load} s_{11}^E l \\
 A_2 &= 2lR_{load} b \left(\left(t_m s_{11}^E + \frac{1}{2} t_p s_{33}^H \right) (k_{31}^2 - 1) s_{11}^E \varepsilon_{33}^T - \frac{1}{2} t_p d_{31,p}^2 s_{33}^H \right) \\
 A_3 &= 2s_{11}^{E^2} t_m t_p + s_{11}^E s_{33}^H t_p^2
 \end{aligned} \tag{7}$$

where b is the PZT layer width, t_p is the PZT layer thickness, $d_{33,m}$ is a longitudinal piezomagnetic constant, $d_{31,p}$ is a transverse piezoelectric constant, t_m is the Terfenol-D layer thickness, s_{11}^E is piezoelectric elastic compliance, l is the PZT layer length, s_{11}^E is piezoelectric elastic compliance, s_{33}^H is piezomagnetic elastic compliance, k_{31} is the piezoelectric electromechanical coupling coefficient, and ε_{33}^T is piezoelectric permittivity [31].

3. Simulations

The approximate analytical method combines the harmonic balance approach and the pseudo-arclength continuation algorithm. Initially, x_i ($i = 1, 2, 3$) in Eq. (1) are represented by the assumption of three harmonic functions as follows:

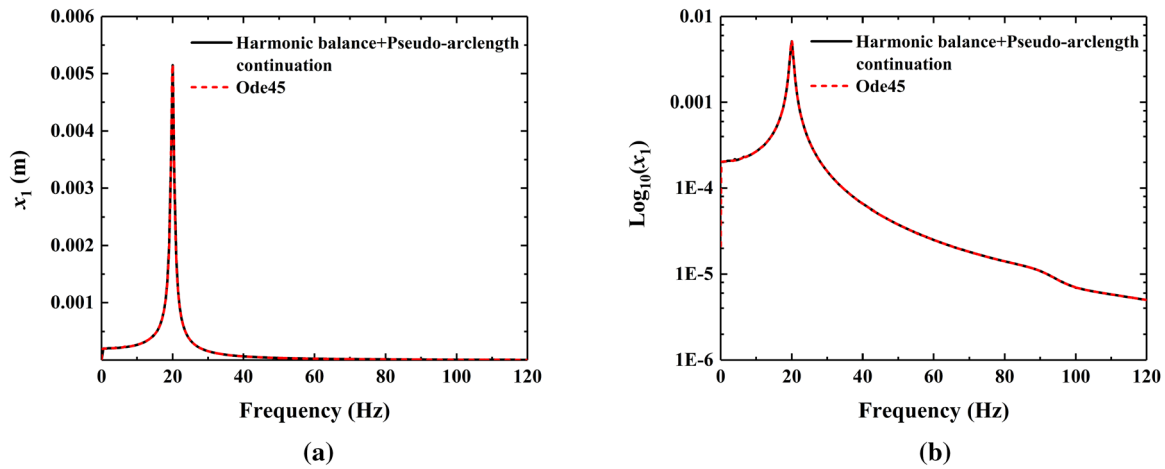


Fig. 2. Comparison of the approximate analytical method with Ode45

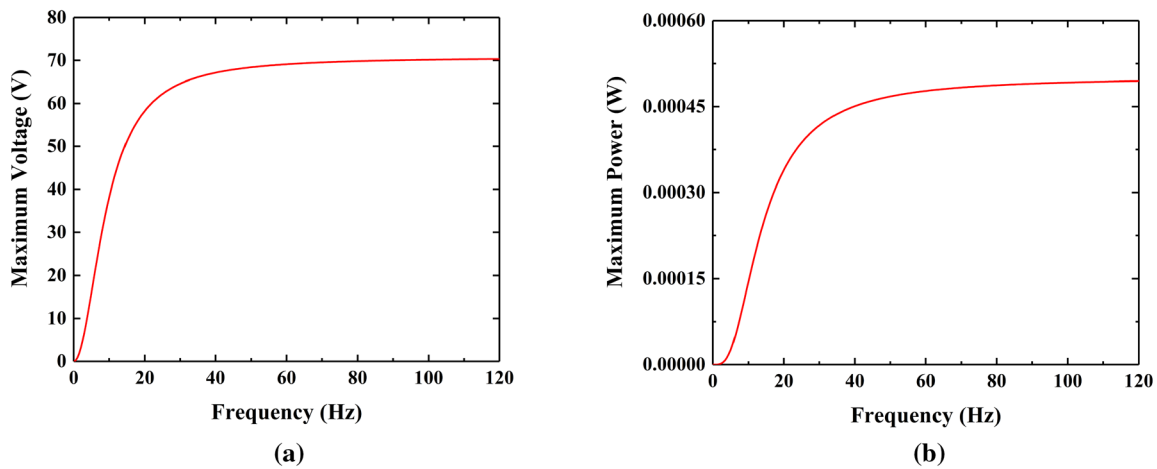
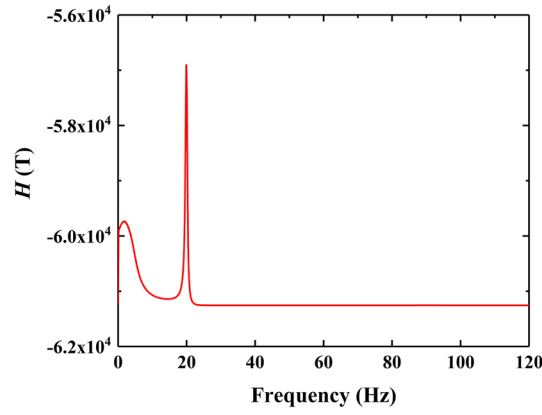
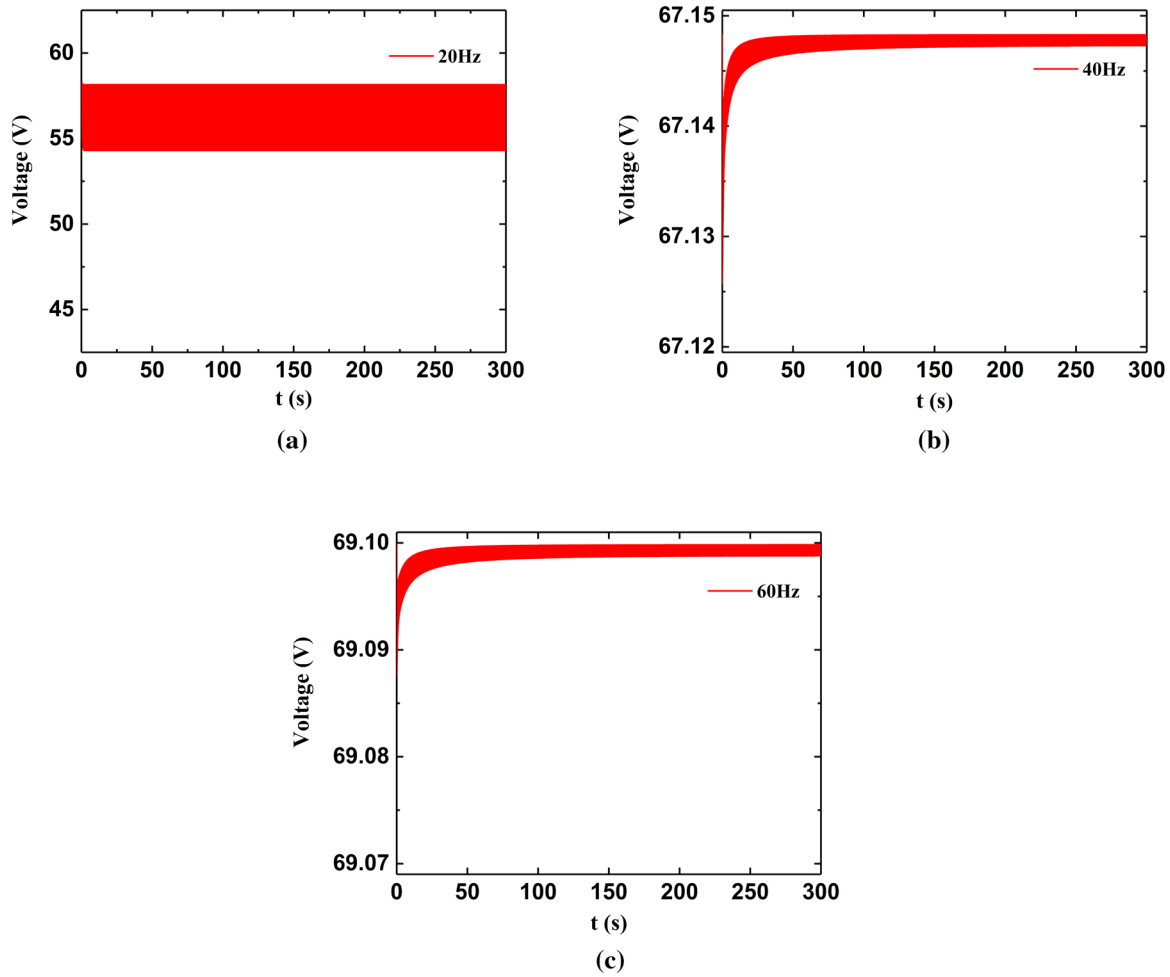


Fig. 3. Harvested energy across a $10^7 \Omega$ load resistance: a maximum voltage and b maximum power

Fig. 4. Magnetic field strength H Fig. 5. Output voltage: a $f = 20$ Hz, b $f = 40$ Hz, and c $f = 60$ Hz

$$\begin{aligned}
 x_1(t) &= a_{11} \cos(\omega t) + b_{11} \sin(\omega t) + a_{31} \cos(3\omega t) + b_{31} \sin(3\omega t) \\
 x_2(t) &= a_{12} \cos(\omega t) + b_{12} \sin(\omega t) + a_{32} \cos(3\omega t) + b_{32} \sin(3\omega t) \\
 x_3(t) &= a_{13} \cos(\omega t) + b_{13} \sin(\omega t) + a_{33} \cos(3\omega t) + b_{33} \sin(3\omega t)
 \end{aligned} \tag{8}$$

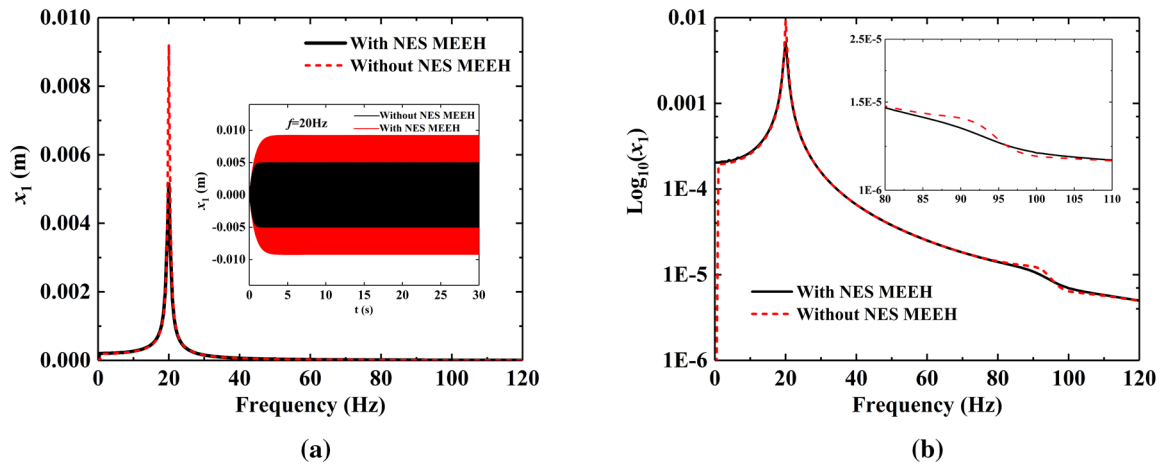


Fig. 6. Comparative analysis of the response with or without NES and MEEH

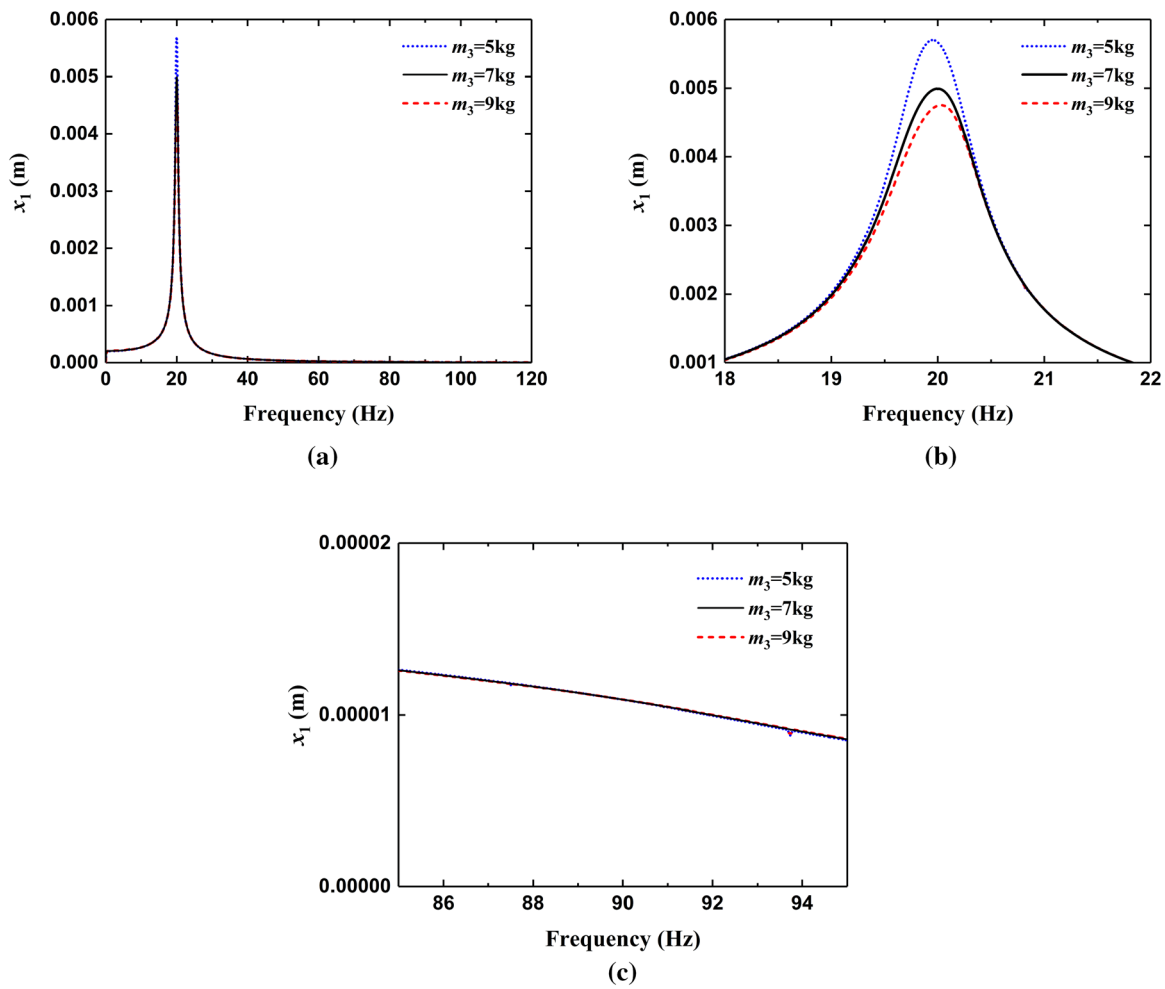


Fig. 7. Amplitude–frequency response curves as the mass changes: a total figure, b enlargement figure near 20 Hz, and c enlargement figure near 90 Hz

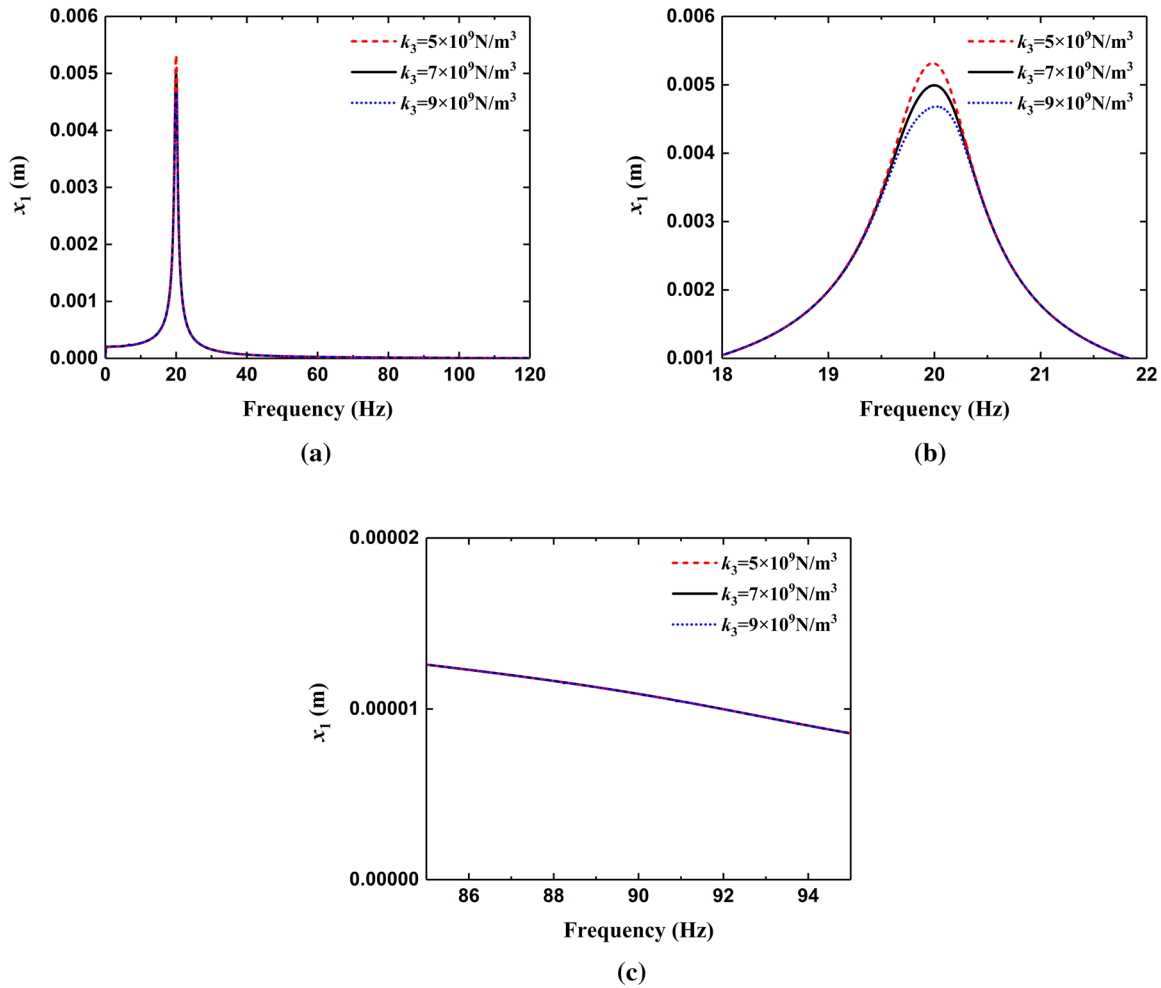


Fig. 8. Amplitude–frequency response curves as the stiffness changes: **a** total figure, **b** enlargement figure near 20 Hz, and **c** enlargement figure near 90 Hz

where $\omega = 2\pi f$ is a variable parameter. By substituting Eq. (8) into Eq. (1), we derive 12 equations. Then, the pseudo-arclength continuation algorithm is used to solve the equations. This study defines vector \boldsymbol{x} consisting of a_{ij} and b_{ij} ($i, j = 1, 2, 3$) to write the 12 equations abstractly as $f(\boldsymbol{x}, \omega) = 0$. We set an extension vector $\boldsymbol{y} = (\boldsymbol{x}, \omega)^T$ and introduce vector \boldsymbol{y}_1 and a fairly small arc length s . We then obtain a new equation, $\|\boldsymbol{y}_1 - \boldsymbol{y}\| - s = 0$. Ultimately, we have 13 equations and 13 unknowns. The Newton–Raphson method is used to solve these equations [34, 35].

The system parameters are $m_1 = 60$ kg, $k_1 = 1.8677 \times 10^6$ N/m, $c_1 = 600$ Ns/m, $m_2 = 12$ kg, $k_2 = 2.1346 \times 10^6$ N/m, $c_2 = 20$ Ns/m, $m_3 = 7$ kg, $k_3 = 7 \times 10^9$ N/m³, $c_3 = 600$ Ns/m [28, 33].

In Fig. 2a, b, the solid black line is the amplitude–frequency response obtained by the harmonic balance approach and pseudo-arclength continuation algorithm, and the dashed red line is the amplitude–frequency response obtained by the fourth-order Runge–Kutta method (Ode45) under 0.3-g base excitation. The results of approximate analysis are nearly consistent with those of the numerical simulation. Figure 2b is an enlargement figure that uses $\log_{10}(x_1)$ as the y -axis. A small peak caused by the second natural frequency of the system is observed at 90 Hz.

3.1. Harvested Energy Analysis

The maximum output voltage and power are shown in Fig. 3, and the magnetic field strength is shown in Fig. 4. The system can harvest energy in the entire frequency range. As the frequency increases, the output voltage value remains stable at 70 V. However, the variation trends of voltage

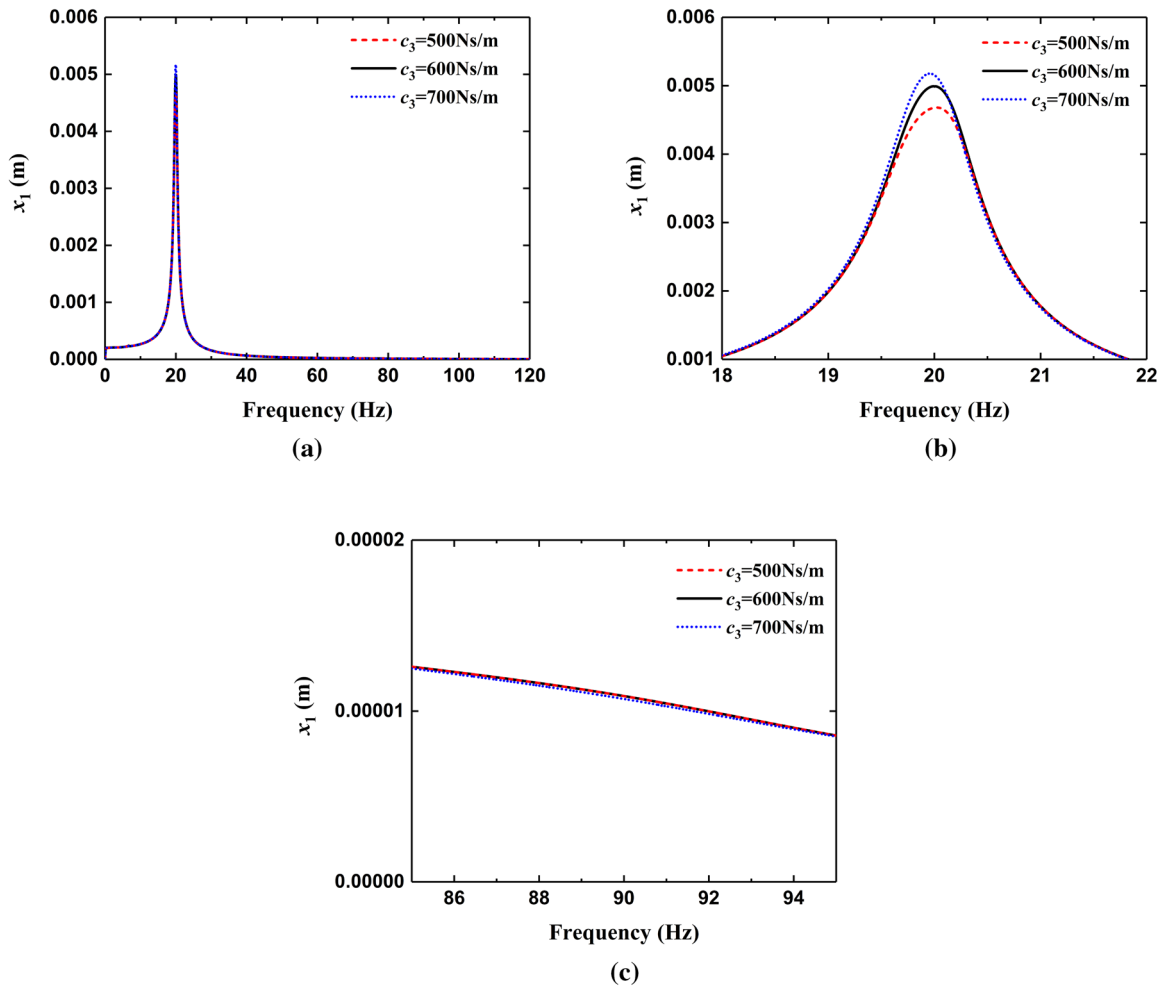


Fig. 9. Amplitude–frequency response curves as the damping changes: **a** total figure, **b** enlargement figure near 20 Hz, and **c** enlargement figure near 90 Hz

and power differ from that of magnetic field strength. This result can be explained by Eq. (6). Voltage is determined by magnetic field strength H , excitation frequency f , resistive load R_{load} , and other parameters with determined values. In Fig. 4, the numerical value of magnetic field strength H varies only slightly, and the value of magnetic field strength is too small for A_1 , A_2 , and A_3 in Eq. (7). Therefore, the change in magnetic field strength has no obvious influence on voltage. Meanwhile, a change in excitation frequency and resistive load changes the voltage considerably. As shown in Fig. 3, output voltage and power increase as the excitation frequency increases across a $10^7 \Omega$ load resistance. In Fig. 5, the voltages at three frequencies are $60 \text{ Hz} > 40 \text{ Hz} > 20 \text{ Hz}$, and the result is consistent with Fig. 3.

3.2. Comparative Analysis of the Response With or Without NES and MEEH

In Fig. 6, the amplitude–frequency responses with or without NES and MEEH are compared under a 0.3-g base excitation. The whole-spacecraft system with NES and MEEH can effectively reduce vibration. The amplitude of the system decreases most at 20 Hz, which is the natural system frequency. The peak of the second natural system frequency disappears in Fig. 6b.

4. Parametric Study

The choice of parameters is crucial to system performance. In this work, the variations in base excitation amplitude A_b , NES (m_3 , k_3 , c_3), and resistive load R_{load} of the system are analyzed. The

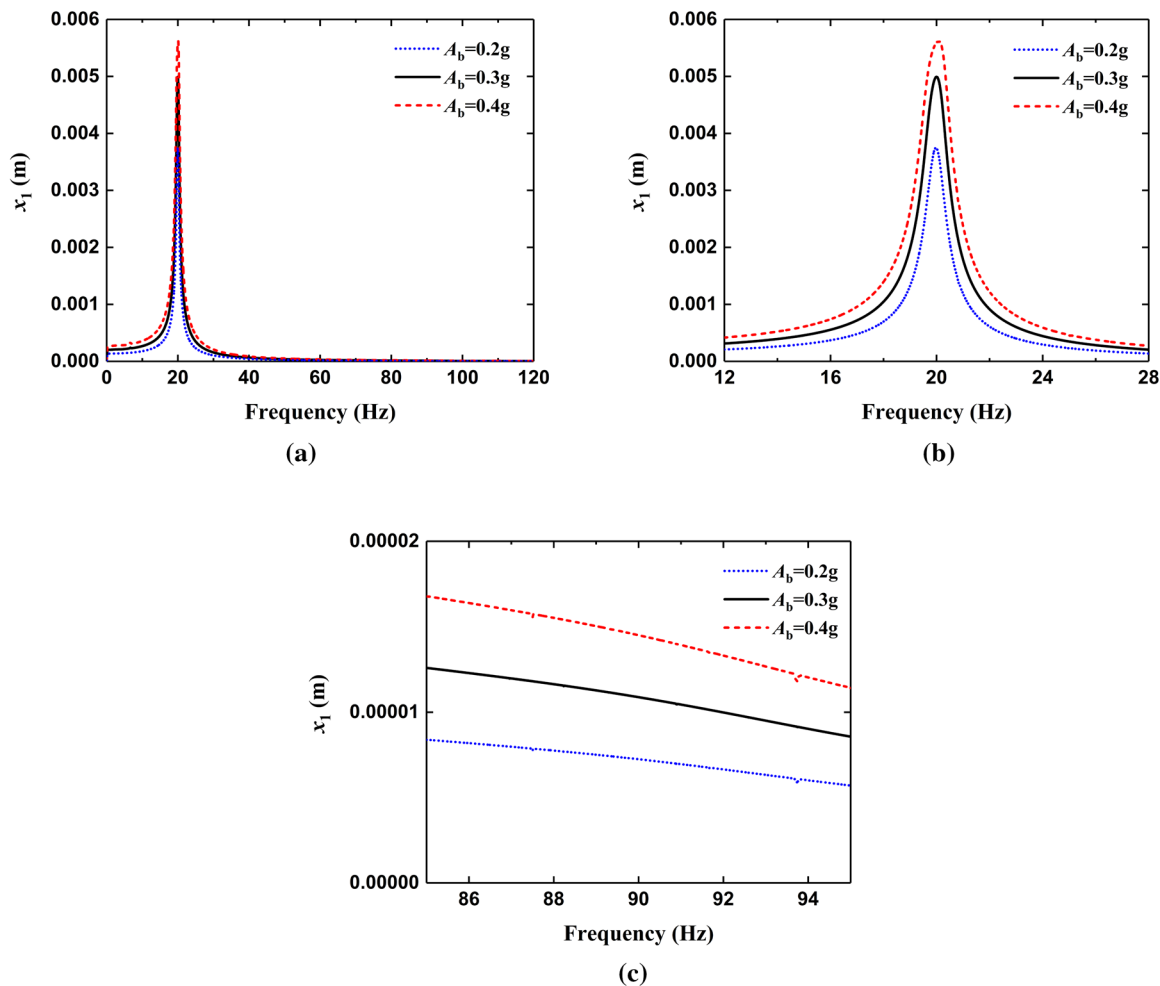


Fig. 10. Amplitude–frequency response curves as the excitation amplitude varies: **a** total figure, **b** enlargement figure near 20 Hz, and **c** enlargement figure near 90 Hz

influence of the change in m_3 on the vibration of the system is examined firstly. Figure 7 depicts the relationship between the amplitude frequency response and NES mass m_3 , with the values of other parameters unchanged. With the increase in NES mass, the response amplitude decreases near 20 Hz and hardly changes at a high frequency. When the value of NES mass is larger, the effect of reducing vibration becomes smaller. As reported in the previous section, the parameters of NES and the base excitation amplitude exert nearly no effect on voltage. Hence, the voltage change is not discussed here.

In Fig. 8, the effect of the variation of NES stiffness coefficient k_3 on the amplitude frequency response is compared. When NES stiffness coefficient k_3 increases, the response amplitude decreases near 20 Hz. Figure 8c is an enlargement figure near 90 Hz, where the amplitude is almost unchanged.

The effects of different NES damping coefficients c_3 on the amplitude frequency response are presented in Fig. 9. The effect of NES damping coefficient on amplitude is different from NES mass and NES stiffness coefficient. The response amplitude increases when NES damping coefficient increases near 20 Hz but hardly changes at a high frequency.

Figure 10 shows the effect of the change in acceleration excitation amplitude A_b on the amplitude frequency response. The effect of A_b on the amplitude is very obvious at low frequencies. The response amplitude increases when excitation amplitude A_b increases near 20 Hz but hardly changes at a high frequency.

In Fig. 11, as base excitation f increases, the output voltage increases. When resistive load R_{load} increases, the output voltage increases at low frequencies. After the frequency is greater than 40 Hz, the

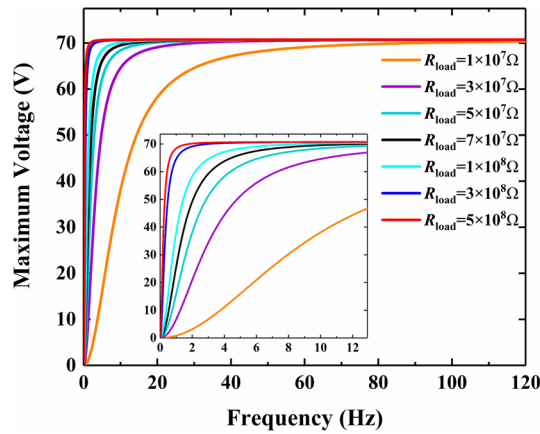


Fig. 11. Maximum voltage curves as the resistive load varies

change of resistive load has little effect on the voltage. The voltage changes very little when resistive load exceeds $1 \times 10^8 \Omega$. The two curves of $R_{\text{load}} = 3 \times 10^8 \Omega$ and $R_{\text{load}} = 5 \times 10^8 \Omega$ are very close, and the highest voltage 70 V can be harvested at low frequencies in these two cases. Therefore, the optimal resistance range is selected as $3 \times 10^8 \Omega - 5 \times 10^8 \Omega$.

5. Conclusion

We propose a new integrated device that combines NES and MEEH to achieve whole-spacecraft vibration reduction and energy harvesting. The dynamic equation of the system is analyzed with an approximate analytical method that combines the harmonic balance approach and pseudo-arclength continuation algorithm. The results are then compared with those of the Runge–Kutta algorithm for numerical simulation. The dynamic response, output voltage, and output power of the system after reaching the steady-state response under acceleration excitation are also calculated.

The following conclusions are derived.

- (1) The integration of NES and MEEH can effectively reduce system vibration while harvesting large amounts of electrical energy over a wide range of frequencies.
- (2) The approximate analytical solution of the dynamic equation obtained by the harmonic balance approach and pseudo-arclength extension algorithm is nearly consistent with the Runge–Kutta algorithm solution.
- (3) The harvested electrical energy is inconsistent with the change in magnetic field strength. The harvested electrical energy increases as the excitation frequency and resistive load increase because the influence of magnetic field strength on voltage is extremely small.

Acknowledgements. This work was supported by the National Natural Science Foundation of China (Project No. 11772205), the Training Project of Liaoning Provincial Higher Education Institutions in Domestic and Overseas (Project No. 2018LNGXGJWPY-YB008), and the Scientific Research Fund of Liaoning Provincial Education Department (Project No. L201703).

References

- [1] Wilke PS, Johnson CD, Fosness ER. Whole-spacecraft passive launch isolation. *J Spacecr Rockets*. 1998;35(5):690–4.
- [2] Johnson CD, Wilke PS, Darling KR. Multi-axis whole-spacecraft vibration isolation for small launch vehicles. *Proc SPIE*. 2001;4331:153–61.
- [3] Liu LK, Zheng GT, Huang WH. Octo-strut vibration isolation platform and its application to whole spacecraft vibration isolation. *J Sound Vib*. 2006;289(4–5):726–44.
- [4] Liu LK, Liang L, Zheng GT, Huang WH. Dynamic design of octostrut platform for launch stage whole-spacecraft vibration isolation. *J Spacecr Rockets*. 2005;42(4):654–62.
- [5] Hu Q, Cao J, Zhang Y. Robust backstepping sliding mode attitude tracking and vibration damping of flexible spacecraft with actuator dynamics. *J Aerosp Eng*. 2009;22(2):139–52.

- [6] Vakakis AF, McFarland DM, Bergman LA, Manevitch LI, Gendelman O. Isolated resonance captures and resonance capture cascades leading to single-or multi-mode passive energy pumping in damped coupled oscillators. *J Vib Acoust.* 2004;126(2):235–44.
- [7] Vakakis AF. Inducing passive nonlinear energy sinks in vibrating systems. *J Vib Acoust.* 2001;123(3):324–32.
- [8] Lu Z, Wang Z, Zhou Y, Lu X. Nonlinear dissipative devices in structural vibration control: a review. *J Sound Vib.* 2018;423:18–49.
- [9] Vakakis AF, Gendelman O. Energy pumping in nonlinear mechanical oscillators ii: resonance capture. *J Appl Mech.* 2001;68(1):42–8.
- [10] Georgiades F, Vakakis AF, Kerschen G. Broadband passive targeted energy pumping from a linear dispersive rod to a lightweight essentially non-linear end attachment. *Int J Non-Linear Mech.* 2007;42(5):773–88.
- [11] Ahmadabadi ZN, Khadem SN. Nonlinear vibration control of a cantilever beam by a nonlinear energy sink. *Mech Mach Theory.* 2012;50:134–49.
- [12] Chen JE, Zhang W, Yao MH, Liu J. Vibration suppression for truss core sandwich beam based on principle of nonlinear targeted energy transfer. *Compos Struct.* 2017;171:419–28.
- [13] Gourc E, Michon G, Seguy S, Berlioz A. Experimental investigation and design optimization of targeted energy transfer under periodic forcing. *J Vib Acoust.* 2014;136(2):021021.
- [14] Zang J, Chen LQ. Complex dynamics of a harmonically excited structure coupled with a nonlinear energy sink. *Acta Mech Sin.* 2017;33(4):801–22.
- [15] Dai HL, Abdelkefi A, Wang L. Usefulness of passive non-linear energy sinks in controlling galloping vibrations. *Int J Non-Linear Mech.* 2016;81:83–94.
- [16] Haris A, Motato E, Mohammadpour M, Theodossiades S, Rahnejat H, O'Mahony M, Vakakis AF, Bergman LA, McFarland DM. On the effect of multiple parallel nonlinear absorbers in palliation of torsional response of automotive drivetrain. *Int J Non-Linear Mech.* 2017;96:22–35.
- [17] Yang B, Lee C, Xiang W, Xie J, He JH, Kotlanka RK, Low SP, Feng H. Electromagnetic energy harvesting from vibrations of multiple frequencies. *J Micromech Microeng.* 2009;19(3):035001.
- [18] Torres EO, Rincón-Mora G. Electrostatic energy-harvesting and battery-charging CMOS system prototype. *IEEE Trans Circuits Syst I Regul Pap.* 2009;56(9):1938–48.
- [19] Li P, Wen Y, Huang X, Yang J, Wen J, Qiu J, Zhu Y, Yu M. Wide-bandwidth high-sensitivity magneto-electric effect of magnetostrictive/piezoelectric composites under adjustable bias voltage. *Sens Actuators A Phys.* 2013;201:164–71.
- [20] Ferrari M, Ferrari V, Guizzetti M, Andò B, Baglio S, Trigona C. Improved energy harvesting from wideband vibrations by nonlinear piezoelectric converters. *Procedia Chem.* 2009;1(1):1203–6.
- [21] Tao K, Tang L, Wu J, Lye SW, Chang H, Miao J. Investigation of multimodal electret-based mems energy harvester with impact-induced nonlinearity. *J Microelectromech Syst.* 2018;27(2):276–88.
- [22] Zhou S, Chen W, Malakooti MH, Cao J, Inman DJ. Design and modeling of a flexible longitudinal zigzag structure for enhanced vibration energy harvesting. *J Intell Mater Syst Struct.* 2017;28(3):367–80.
- [23] Liu H, Gudla S, Hassani FA, Heng CH, Lian Y, Lee C. Investigation of the nonlinear electromagnetic energy harvesters from hand shaking. *IEEE Sens J.* 2015;15(4):2356–64.
- [24] Zhou S, Zuo L. Nonlinear dynamic analysis of asymmetric tristable energy harvesters for enhanced energy harvesting. *Commun Nonlinear Sci Numer Simul.* 2018;61:271–84.
- [25] Chtiba MO, Choura S, Nayfeh AH, El-Borgi S. Vibration confinement and energy harvesting in flexible structures using collocated absorbers and piezoelectric devices. *J Sound Vib.* 2010;329(3):261–76.
- [26] Ahmadabadi ZN, Khadem SE. Nonlinear vibration control and energy harvesting of a beam using a nonlinear energy sink and a piezoelectric device. *J Sound Vib.* 2014;333(19):4444–57.
- [27] Fang ZW, Zhang YW, Li X, Ding H, Chen LQ. Integration of a nonlinear energy sink and a giant magnetostrictive energy harvester. *J Sound Vib.* 2017;391:35–49.
- [28] Fang ZW, Zhang YW, Li X, Ding H, Chen LQ. Complexification-averaging analysis on a giant magnetostrictive harvester integrated with a nonlinear energy sink. *J Vib Acoust.* 2017;140(2):021009.
- [29] Kremer D, Liu K. A nonlinear energy sink with an energy harvester: transient responses. *J Sound Vib.* 2014;333(20):4859–80.
- [30] Kremer D, Liu K. A nonlinear energy sink with an energy harvester: harmonically forced responses. *J Sound Vib.* 2017;410:287–302.
- [31] Zhu Y, Zu JW, Guo L. A magnetolectric generator for energy harvesting from the vibration of magnetic levitation. *IEEE Trans Magn.* 2012;48(11):3344–7.
- [32] Dai X, Wen Y, Li P, Yang J, Zhang G. Modeling, characterization and fabrication of vibration energy harvester using Terfenol-D/PZ. *Sens Actuators A Phys.* 2009;156(2):350–8.

- [33] Yang K, Zhang YW, Ding H, Yang TZ, Li Y, Chen LQ. Nonlinear energy sink for whole-spacecraft vibration reduction. *J Vib Acoust.* 2017;139(2):021011.
- [34] Ding H, Zhu MH, Chen LQ. Nonlinear vibration isolation of a viscoelastic beam. *Nonlinear Dyn.* 2018;92(2):325–49.
- [35] Ding H, Tang YQ, Chen LQ. Frequencies of transverse vibration of an axially moving viscoelastic beam. *J Vib Control.* 2017;23(20):3504–14.